Clays and Clay Minerals, Vol. 58, No. 4, 522–531, 2010.

STRUCTURAL CHANGE IN CELADONITE AND *CIS*-VACANT ILLITE BY ELECTRON RADIATION IN TEM

TOSHIHIRO KOGURE[1] AND VICTOR A. DRITS[2]

[1] Department of Earth and Planetary Science, Graduate School of Science, The University of Tokyo, 7-3-1 Hongo, Bunkyo-ku, Tokyo, 113-0033, Japan
[2] Geological Institute of the Russian Academy of Sciences, Pyzhevsky per 7, Moscow, Russia

Abstract—High-resolution transmission electron microscopy (HRTEM) images of two dioctahedral micas, celadonite and *cis*-vacant (*cv*) illite, were examined in detail to understand the effects of electron radiation on their structures during image acquisition. Celadonite, a dioctahedral mica with Fe and Mg as major octahedral cations, originally has a *trans*-vacant (*tv*) octahedral sheet but the contrast in the high-resolution transmission electron microscopy (HRTEM) images indicates a different cation distribution in the sheet. Furthermore, the β angle for the 1*M* polytype derived from the HRTEM images is ~98.5º, which is considerably smaller than that (~100.5º) reported for celadonite. In previous works, cation migration from the *tv* to *cv*-like configurations and a decrease in the β angle after dehydroxylation of celadonite/glauconite by heating were reported. The same phenomenon, dehydroxylation and subsequent cation migration, probably occurs by electron radiation in TEM. However, the new cation-distribution models derived from HRTEM images along the [100] and [110] directions are not in agreement. On the other hand, the contrast in a number of HRTEM images from an illite specimen in which *cv*-illite is dominant is the same as that for the *tv*-dioctahedral layer. This result is also interpreted as cation migration accompanied by dehydroxylation in TEM, as reported in heated *cv*-illite. The increased β angle (~102.5º) from that in the natural state (101.5º) estimated from the HRTEM images also supports this interpretation. This phenomenon is a large obstacle to the investigation of phyllosilicates containing Al-rich *cv* and Mg,Fe-rich *tv* 2:1 layers, using HRTEM.

Key Words—Celadonite, *Cis*-vacant, Illite, TEM, *Trans*-vacant.

INTRODUCTION

Although the crystal structures of major minerals have already been determined and refined, the structures of minerals occurring as fine particles only are still not understood completely, *e.g*. the cation distribution in the octahedral sheet of some dioctahedral 2:1 phyllosilicates. In general, the octahedral sheet in a 2:1 layer contains three crystallographically independent sites (M1, M2, and M3, Ferraris and Ivaldi, 2002) which differ in the arrangement of coordinating OH groups: the OH groups lie across the space diagonally ('*trans*' configuration) at the M1 site whereas the OH groups form a shared edge with a neighboring octahedron ('*cis*' configuration) at the M2 and M3 sites (these two sites are often related to each other by a symmetry plane in the mica structure and referred to as M2 only). The crystal structures of muscovite, paragonite, margarite, pyrophyllite, *etc*., for which sufficiently large, high-quality crystals for single-crystal structure analyses are available, adopt a *trans*-vacant (*tv*) octahedral sheet where the *trans*-octahedron is vacant. Expecting other fine-grained dioctahedral 2:1 phyllosilicates (*e.g.* illite and dioctahedral smectite) to have a similar cation distribution in their octahedral sheets is not unreasonable. Mering and Oberlin (1971), however, first proposed that a montmorillonite specimen adopts the vacancy sites not at the *trans*-octahedra, but at the *cis*-octahedra (*cis*-vacant: *cv*). Drits *et al.* (1984) were the first to deduce the unit-cell parameters and atomic coordinates for a one-layer monoclinic (1*M*) *cv*-illite model. Those authors calculated powder X-ray diffraction (XRD) patterns for periodic 1*M*-*cv* illite, as well as for models in which *tv* and *cv* layers are interstratified, and formulated diffraction criteria for the identification of these illite varieties. Tsipursky and Drits (1984) studied numerous dioctahedral smectites and revealed a wide variety of occupancies of the *cis*- and *trans*-octahedral sites including *cv* (most montmorillonites) and *tv* (nontronites, beidellites, and some montmorillonites) samples, as well as those consisting of interstratified *cv* and *tv* layers. Zvyagin *et al.* (1985) were the first to describe a monomineral Al-rich 1*M*-*cv* mica sample, and Reynolds (1993) demonstrated for the first time that illite fundamental particles in mixed-layer illite-smectite (I-S) consist either of *tv* or *cv* layers, or both layer types are interstratified in these particles. Since then, the occurrences of the *cv* layer in dioctahedral smectites, illites, and I-S in various geological environments have been reported by numerous authors (*e.g*. Drits *et al.*, 1993; McCarty and Reynolds, 1995,

* E-mail address of corresponding author:
kogure@eps.s.u-tokyo.ac.jp
DOI: 10.1346/CCMN.2010.0580407

https://doi.org/10.1346/CCMN.2010.0580407 Published online by Cambridge University Press

2001; Reynolds and Thomson, 1993; Lee, 1996; Lanson *et al.* , 1996; Zhukhlistov *et al.,* 1996; Drits *et al.*, 1996; Altaner and Ylagan, 1997; Cuadros and Altaner, 1998a, 1998b; Ylagan *et al.*, 2000; Lindgreen *et al.*, 2000, 2002; Sainz-Diaz *et al.,* 2001; Drits, 2003 and references therein; Drits *et al.*, 2002, 2004, 2006, 2007; McCarty *et al.,* 2008; Emmerich *et al*., 2009; Wolters *et al*., 2009).

Details of the structures of phyllosilicates containing the *cv* layers are still somewhat obscure, however. For instance, the *cv* layer has only a two-fold axis of symmetry in its structure, which results in the existence of enantiomers. The distribution of these enantiomeric domains in a crystal is unclear. A similar question as to how *cv* and *tv* layers are interstratified in specimens containing both layers is easily raised. A solution to answer these questions must be to examine these specimens using high-resolution transmission electron microscopy (HRTEM) with the beam direction parallel to the layers. As shown later, discrimination of the *cv* and *tv* layers from HRTEM contrasts, using a conventional TEM, is theoretically possible. However, no such report of HRTEM contrasts showing the *cv* layer in illite or smectite specimens in which the *cv* layers are dominant has been made. Celadonite and glauconite, dioctahedral micas with trivalent Fe and Mg as major octahedral cations, originally have a *tv* octahedral sheet but the HRTEM images indicated a different cation distribution (Kogure *et al.*, 2008b). The present paper describes these results in detail and the origin of the discrepancy between expected and actually recorded images is discussed.

SAMPLES AND METHODS

The celadonite specimens investigated were from Taiheizan, Akita, Japan (Kimbara and Shimoda, 1973) and from Krivoi Rog, Ukraine (Zhukhlistov *et al.*, 1977). The reported formulae are:

Taiheizan:
$(K_{0.817}Na_{0.176})(Al_{0.159}Fe^{3+}_{1.066}Fe^{2+}_{0.140}Mg_{0.666})(Si_{3.721}Al_{0.279})O_{10}(OH)_2$

Krivoi Rog:
$(K_{0.83}Na_{0.01}Ca_{0.04})(Al_{0.05}Fe^{3+}_{1.15}Fe^{2+}_{0.36}Mg_{0.41}Ti_{0.01})(Si_{3.94}Al_{0.06})O_{10}(OH_{1.99}F_{0.01})$

Structural studies of celadonite samples reported that they consist of *tv* layers (Tsipursky and Drits, 1986; Zhukhlistov, 2005). In fact, no difference was observed between the two specimens with respect to the results described in the present study. The illite specimen was that from hydrothermal alterations around uranium deposits located in the Athabasca basement, Saskatchewan, Canada (sample 90488 in Drits *et al*., 1993) with the reported formula: $(K_{0.72}Na_{0.01}Ca_{0.01})(Al_{1.85}Mg_{0.15}Fe_{0.04})(Si_{3.27}Al_{0.73})O_{10}(OH)_2$. The powder XRD pattern suggested that the illite specimen is a mixture of *cv*-1*M* and *tv*-1*M* crystallites with *cv*-1*M* dominant. The specimen is referred to hereafter as 'Canada illite.'

Specimens for TEM examination were prepared following Kogure (2002). In short, the sample powder was embedded in epoxy resin between two glass slides. After hardening, the glass slides were cut into laths ~1 mm thick using a diamond wheel. The laths were thinned to ~50 μm by mechanical grinding and then argon ion milled. The HRTEM examination was performed at 200 kV using a JEOL JEM-2010 UHR with a nominal point resolution of ~2.0 Å. The HRTEM images were recorded on films or with a Gatan MSC 794 bottom-mounted CCD camera. The HRTEM images were taken from sufficiently thin regions of the specimens and by adjusting the defocus value to record the contrast that corresponds to the projected potential of the crystal structure (Kogure, 2002). Noisy contrast, from amorphous materials superimposed on the crystal contrasts, was removed using a Wiener-filter (Marks, 1996; Kilaas, 1998) developed by K. Ishizuka (HREM Research, Inc.) and implemented with the Gatan *DigitalMicrograph* version 3.10.0 (Kogure *et al*., 2008a). In order to measure accurate angles between two lattice fringes in HRTEM images, elliptical distortion in the images caused by lens aberration was corrected with the values for elliptical distortion (Capitani *et al.*, 2006) estimated from the [110] HRTEM images of a silicon single crystal. Adobe *PhotoShop*® was used for the distortion correction of the recorded images. The angles between crossed lattice fringes in the images were measured using *Digital Micrograph*®. The celadonite specimen was also examined using a high-angle annular dark-field scanning transmission electron microscopy (HAADF-STEM) with a spherical aberration (Cs) corrector. The electron microscope used was a JEOL JEM-2100F with a CEOS GmbH hexapole Cs-corrector for the probe-forming lens, and a Schottky-type field emission electron gun operated at 200 kV. The beam convergence semi-angle of the probe was 25 mrad. The detection semi-angle of the HAADF detector was between 80 (inner) and 200 mrad (outer). Finally, multi-slice simulation for HRTEM contrasts was performed using *MacTempas*® (Total Resolution Co., Berkeley, California, USA). The contrasts were simulated using parameters for the JEM-2010 UHR electron microscope, *i.e.* spherical aberration coefficient of 0.5 mm, spread of focus half width of 10 nm, beam convergence of 0.5 mrad, the objective aperture corresponded to 7.0 nm^{-1}, and acceleration voltage of 200 kV.

RESULTS

HRTEM images of celadonite

An HRTEM image from a packet of layers in Taiheizan celadonite was recorded along the [1$\bar{1}$0] or

https://doi.org/10.1346/CCMN.2010.0580407 Published online by Cambridge University Press

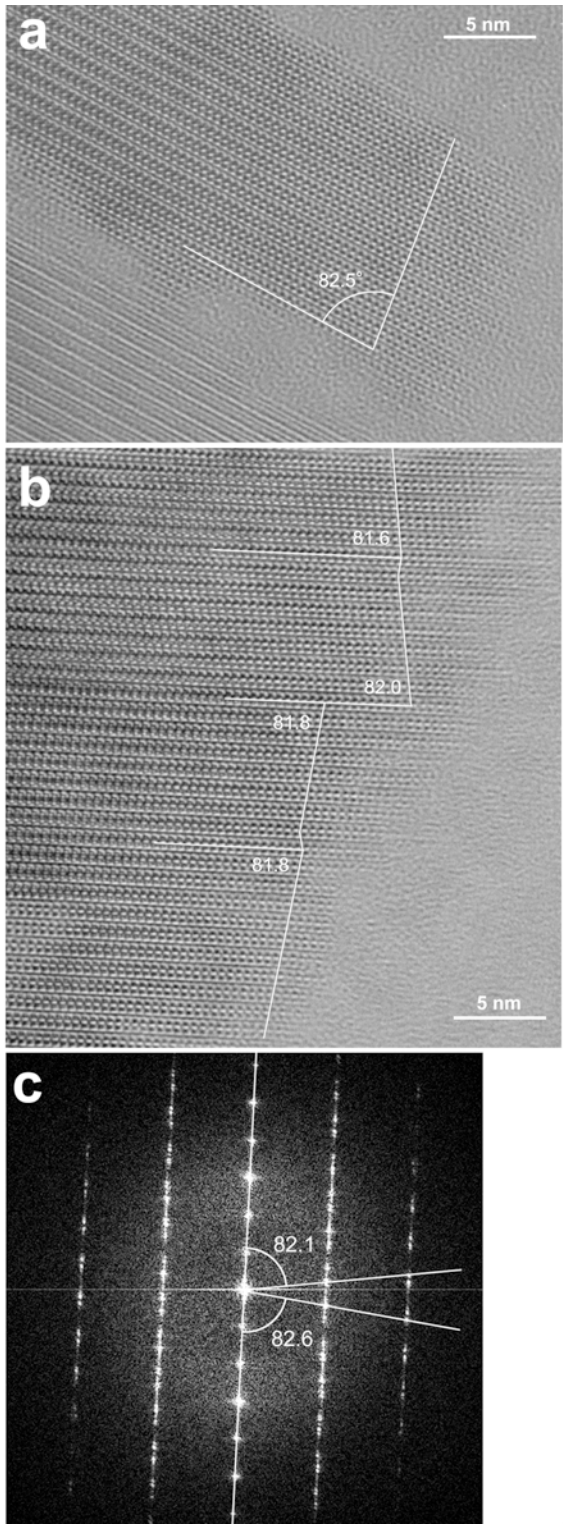


Figure 1. (a) HRTEM image from a thin crystallite of Taiheizan celadonite, recorded along the [1$\bar{1}$0] direction. The angle between the (001) and (110) planes is shown. (b) HRTEM image of a twinned area of Taiheizan celadonite and (c) its Fourier transform. The angle between the (001) and (110) planes for each of twin domains is shown in both figures.

[$\bar{1}\bar{1}$0] direction ([1$\bar{1}$0] is assumed in the following discussion) (Figure 1a). For geometric measurements, the image distortion was corrected and the noisy contrast in the image was reduced using the Wiener-filter (local 2D method, see Kogure *et al*., 2008a). The angle between the (001) and (110) planes, expressed as (001)^(110), in the image is ~82.5º. In another HRTEM image (Figure 1b) and its Fourier transform (Figure 1c) the stacking disorder was observed. This disorder is presumed to be the 180º rotational twins commonly observed in celadonite, as reported by Kogure *et al*. (2008b). The measured (001)^(110) from the image and Fourier transform varied between 81.6 and 82.6º, probably owing to the limited pixel numbers of the digitized image. These angles should be 80.64º, if calculated from the cell parameters determined for the Taiheizan celadonite (Kogure *et al*, 2008b). These large deviations of the measured angles cannot be attributed to misorientation of the crystals because the images show the HRTEM contrast of 1*M* micas along the exact zone axes (Kogure, 2002). The β angle of this celadonite (Kogure *et al*., 2008b) is 100.78(8)º and those reported for other celadonite specimens (*e.g.* Tsipursky and Drits, 1986; Muller *et al*., 2000a; Zhukhlistov, 2005) are also 100.4–100.7º. With the assumption that the a^*/b^* ratio is ~$\sqrt{3}$, (001)^(110) is expressed as $\cos^{-1}(-\sqrt{3}/2 \times \cos\beta)$. Hence, the angle of 82.0º for (001)^(110), for example, corresponds to β = 99.2º, ~1.5º smaller than reported previously.

The HRTEM image of the Krivoi Rog celadonite along the [100] direction also shows an unexpected contrast at each 2:1 layer (Figure 2a). The image shows a symmetrical feature with the mirror plane normal to the *b* axis, indicating a monoclinic system (see Kogure, 2002, for the correspondence between the HRTEM contrast and the structure of the 2:1 layer). In a portion of the image (Figure 2b), three-line profiles of the contrast on the two tetrahedral (T1 and T2) sheets and the octahedral (O) sheet between them were measured using *DigitalMicrograph* (Figure 2c). The phase of the oscillation curve for the contrast at the O sheet is inversed against those at the T1 and T2 sheets. This is completely contradictory to the contrast for the *tv*-dioctahedral structure of celadonite, as shown by the simulated results for various cation distributions in the octahedral sheet (Figure 3). The composition with respect to octahedral cations corresponds to that reported for Krivoi Rog celadonite and the atomic coordinates follow those reported by Zhukhlistov (2005). The site occupancy in Figure 3a corresponds to the *tv*-layer and that in Figure 3b to the *cv*-layer with one of the two *cis*-sites completely empty. Clearly the experimental contrast in Figure 2 does not match that of the *tv*- or *cv*-layers. On the other hand, Figure 3c is the result for the model where the M1 site is fully occupied and the M2 and M3 sites are half occupied. This occupancy explains the experimental contrast well. Finally, Figure 3d is the

https://doi.org/10.1346/CCMN.2010.0580407 Published online by Cambridge University Press

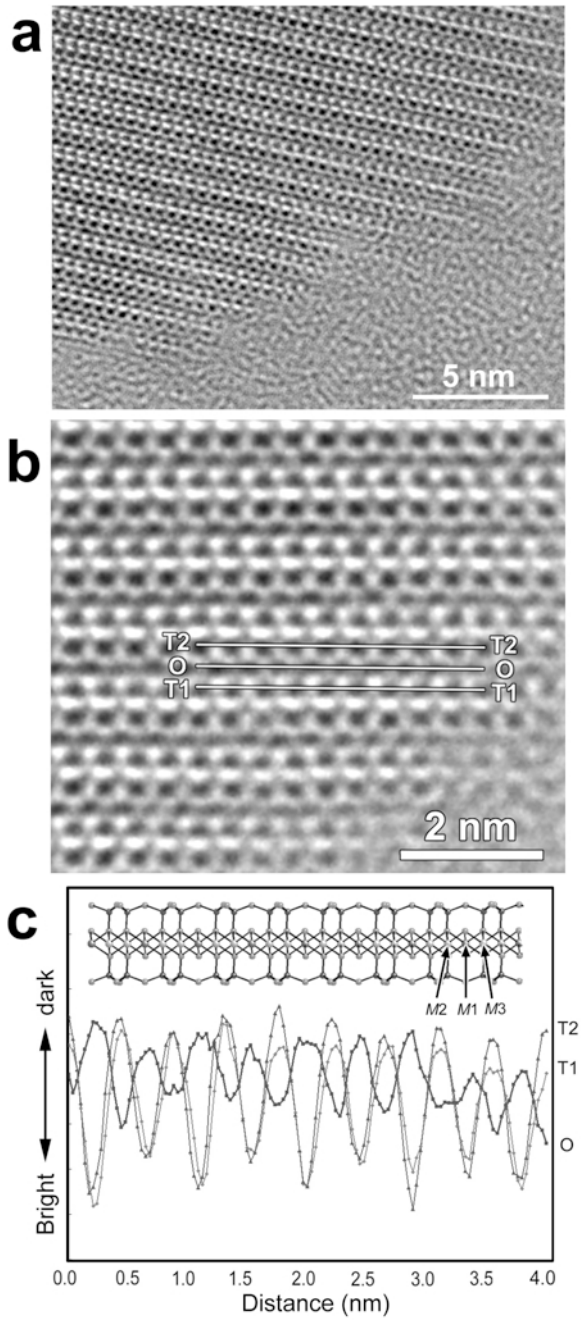


Figure 2. (a) HRTEM image of Krivoi Rog celadonite along the [100] direction. (b) A magnified portion of the image in (a) showing the lines used to measure the intensity profiles of the contrast. (c) Line intensity profiles along the two tetrahedral sheets (T1, T2) and octahedral sheet (O) between them, as shown in (b). The structure model of the 2:1 layer viewed along the [100] direction is shown in (c) for comparison.

result for the model in which the three sites are equally occupied (one third are vacant for all site types) but the M1 site is occupied with Fe only. In this case, the relative amplitude of the oscillation at the O sheet compared to those of the T sheets is weaker than in the experimental image. In conclusion, the experimental HRTEM contrast in Figure 2 is explained well with the M1 site fully occupied. This result is also confirmed by the Cs-corrected HAADF-STEM image from the same specimen (Figure 4) in which the image contrast is approximately proportional to Z^2, the average of the squared atomic numbers of atoms in each atomic column (Pennycook and Jesson, 1990). Its resolution using the Cs-corrector for the probe-forming lens reaches close to 0.1 nm (Krivanek *et al.*, 1999). Although the original image (Figure 4a) is too noisy, the filtered image (Figure 4b) resolves all cation columns along the [100] direction. In the processed image, the three octahedral sites are separated from each other by ~0.16 nm. Among these three sites, the contrast at the M1 site is the brightest and those at the M2 and M3 sites are weaker, in agreement with the results derived from the HRTEM image in Figures 2 and 3.

The HRTEM contrast at the octahedral sheet, recorded along the [1$\bar{1}$0] direction, cannot be explained, however, with this occupancy model (Figure 5). If the three-line profiles in a 2:1 layer are measured (Figure 5b), the maximum of the curve at the O sheet locates at the M2 site. The contrast is well explained by the cation distribution in which the M2 site is fully occupied and the M1 and M3 sites are half occupied (Figure 5c). This disagreement of the cation occupancies derived from [100] and [1$\bar{1}$0] HRTEM imaging will be discussed below.

HRTEM images from 'Canada illite'

The HRTEM images from several illite crystallites are shown in Figure 6. The images in Figure 6a–d are those viewed along the [110] direction, and those in Figures 6e–f along the [100] direction. The images in Figures 6c and 6d are the inversions of the original images to make the comparison easier. At first, the HRTEM contrasts in the 2:1 layers in all images clearly corresponded well to the simulated contrast for the *tv*-layer (Figure 6g), where the dark spot forms at the position corresponding to the center between M2 and M3 cation columns in the O sheet. Other images (>10) obtained through the experiment were similar. This seems to contradict the XRD result that *cv*-illite is the dominant phase in this specimen (Drits *et al.*, 1993). Next, the angle between the (001) and (110) planes measured from the images (Figure 5a–d) is 79–80º. This angle corresponds to a 1*M* mica cell with β = 101.5–102.5º which is considerably larger than that (99.2º) for *cv*-1*M* illite reported by Drits *et al.* (1993). Although *cv*-1*M* illite is the dominant phase, the specimen is the mixture of *cv*-1*M* and *tv*-1*M*, and one may suspect that only *tv*-1*M* crystals have been selected during the observation. For instance, during TEM operation larger grains may have been preferred in order to make the setting of the orientation easier, and this might result in the preference of *tv*-1*M* crystallites.

https://doi.org/10.1346/CCMN.2010.0580407 Published online by Cambridge University Press

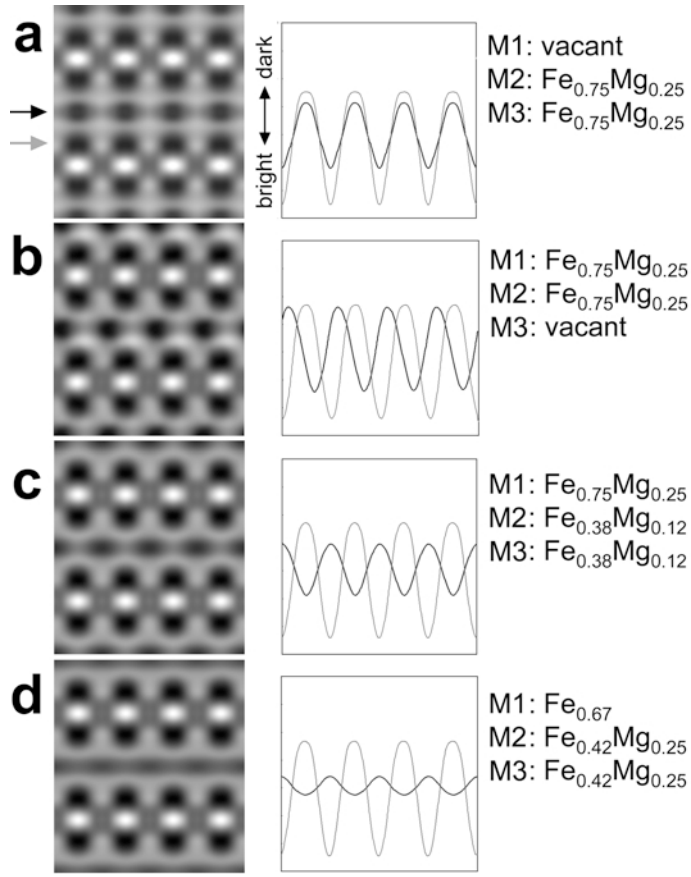


Figure 3. (left) Multi-slice simulation of the HRTEM contrast of celadonite for various occupancies at the three octahedral sites, and (right) the line profiles of contrast at the octahedral sheet (bold) and tetrahedral sheet (thin).The occupancy in (a) corresponds to the natural state of Krivioi Rog celadonite (*trans*-vacant). The thickness and defocus values for the simulation are 2.5 nm and −32 nm, respectively.

However, as described by Drits *et al*. (1993), the XRD patterns from the various grain sizes indicated no size difference between *cv*-1*M* and *tv*-1*M* grains. Hence, the result that no illite particle showed HRTEM contrast corresponding to the *cv*-layer is probably not due to the experimental procedure.

DISCUSSION

The HRTEM contrasts of celadonite do not correspond to the *tv*-1*M* structure and all images from Canada illite showed a contrast corresponding to the *tv*-1*M* structure, although this specimen is supposed to contain *cv*-1*M* illite as the dominant phase. As discussed below, these unexpected results can be explained by the cation migration induced by dehydroxylation in the TEM.

Dioctahedral 2:1 phyllosilicates (pyrophyllite, muscovite, paragonite, *etc*.) lose hydroxyls by heating and a dehydroxylated structure forms topotaxially from the original 2:1 layer (*e.g*. Wardle and Brindley, 1972; Udagawa *et al*., 1974; Comodi and Zanazzi, 2000). For instance, the dehydroxylation of paragonite starts from ~600ºC in air (Comodi and Zanazzi, 2000). Kogure (2007) found that HRTEM images of paragonite are better explained with its dehydroxylated form rather than with the natural state, although the TEM specimen was not heated. This phenomenon was interpreted to mean that electron radiation in the vacuum chamber of the TEM induces dehydroxylation of paragonite, even though the sample is not heated in the beam up to a temperature at which dehydroxylation proceeds in air. On the other hand, cation migration occurs in celadonite and *cv*-illite if they are dehydroxylated by heating (Muller *et al*., 2000a; Drits *et al*., 1995). Celadonite and glauconite (the interlayer-deficient phase of celadonite according to the terminology by Rieder *et al*., 1999) transform from the original *tv* 2:1 layer to a new dehydroxylated 2:1 layer in which the cation (mainly Fe^{3+} and Mg) arrangement is *cv*-like (Muller *at al*., 2000a). Moreover, Muller *at al*. (2000a) reported that this dehydroxylation and subsequent cation migration in celadonite and glauconite accompany the decrease in the β angle from 101º to 99º. Hence, the unexpected HRTEM contrast of the 2:1 layer and the decreased β

https://doi.org/10.1346/CCMN.2010.0580407 Published online by Cambridge University Press

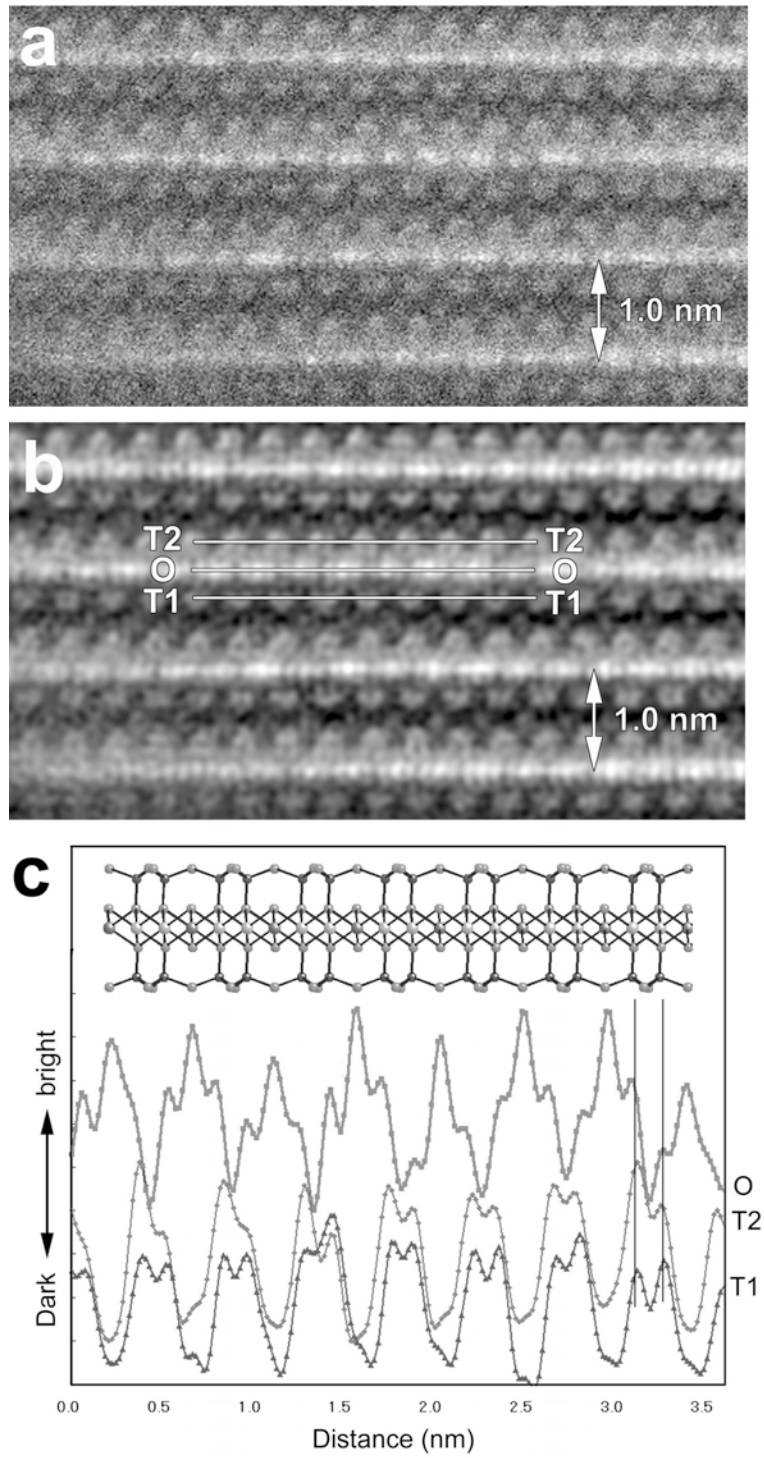


Figure 4. (a) Cs-corrected HAADF-STEM image of Krivoi Rog celadonite recorded along the [100] direction. (b) Filtered image of that in (a), with the lines used to measure intensity profiles of contrast. (c) Line-intensity profiles along the two tetrahedral sheets (T1, T2) with octahedral sheet (O) between them.

angle inferred from the image of celadonite (Figures 1, 2) probably correspond to the dehydroxylated form with cation migration which was induced by electron radiation. Similarly, if *cv*-illite is dehydroxylated by heating, octahedral cations (Al in this case) migrate to form a *tv*-like arrangement, accompanied by an increase in the β angle (Drits *et al.*, 1995). Muller *et al.* (2000b) reported that the structure of *cv*-illite after dehydroxylation and

https://doi.org/10.1346/CCMN.2010.0580407 Published online by Cambridge University Press

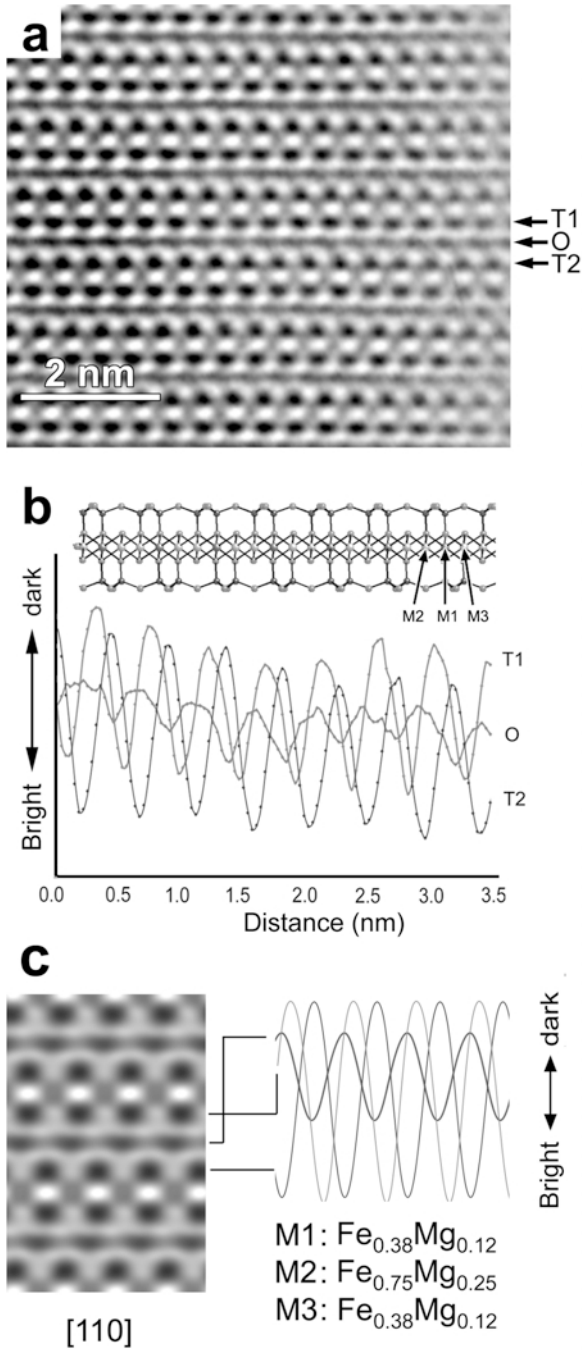


Figure 5. (a) HRTEM image of Krivoi Rog celadonite recorded along the [1$\bar{1}$0] direction. (b) Line-intensity profiles along the T1, T2, and O sheets in (a). (c) Multislice simulation of the HRTEM contrast of celadonite along the [1$\bar{1}$0] direction for cation occupancies shown in the figure. The thickness and defocus values for the simulation are 2.5 nm and −32 nm, respectively.

cation migration by heating is identical to the dehydroxylated *tv*-illite. Hence, the reason that experimental HRTEM images found no *cv*-layers is probably because all *cv*- layers were transformed to a dehydroxylated form with *tv*-like cation arrangement before the recording was made.

The explanation for the origin of cation migration by dehydroxylation in celadonite/glauconite and *cv*-illite was described by Muller *et al*. (2000a) and Drits *et al*. (1995). Dehydroxylation of the 2:1 layer by the reaction $2(OH) \rightarrow H_2O + O_r$ results in five-fold coordination for the former *cis*-sites and six-fold coordination for the former *trans*-site. This five-fold coordination includes a short distance between cations and residual oxygen (O_r) because the height of O_r is at the same level as the cations. To increase this distance, the lateral dimension of the O sheet would need to expand. However, this expansion is limited due to the upper and lower T sheets in the 2:1 layer. In the case of celadonite/glauconite in particular, no margin to expand the O sheet exists because the T sheets are already fully stretched with the ditrigonal rotation angle close to zero (Tsipursky and Drits, 1986; Zhukhlistov, 2005). Consequently, to release this unstable five-fold coordination with a short (Mg, Fe^{3+})−O_r distance, the O sheet is reorganized with migration of some of the cations from the former *cis*-sites to the former *trans*-site. Moreover, the O_r are located with equal probability in either of the sites previously occupied by OH groups, forming shared edges and providing 5-fold coordination for migrated cations (Muller *et al*., 2000a). On the other hand, dehydroxylation of *cv*-illite results in the formation of deformed former *trans*-octahedra (Drits *et al*., 1995). In the octahedron, the Al−O_r distance is so long that O_r is strongly undersaturated with respect to positive charge. This undersaturation may be partly compensated by the movement of Al toward O_r, but the structure is still unstable because complete equalization of the saturation at the anions is not expected with minor movement of the atomic positions (Drits *et al*., 1995). Thus, application of thermal energy or electron radiation should promote the migration of Al at the former *trans*-site to the former *cv*-site, which results in the same structure as a dehydroxylated *tv*-dioctahedral layer.

From these results, recording of the HRTEM images of celadonite and *cv*-illite in their natural state would appear to be very difficult. One possible solution is to minimize electron dose in the recording process of the images. However, a certain amount of electron dose is inevitable for HRTEM recording, which includes setting of the crystal orientation using selected-area electron diffraction (SAED), focus adjustment, and recording on films or CCD cameras. One might expect that at least the recording of diffraction patterns instead of HRTEM images should be possible. Kogure (2007) reported gradual changes in SAED patterns of paragonite during electron radiation, which probably indicated the progress of dehydroxylation. However, in his experimental work on paragonite, a large single crystal was used and a fresh area without beam radiation could be selected after

https://doi.org/10.1346/CCMN.2010.0580407 Published online by Cambridge University Press

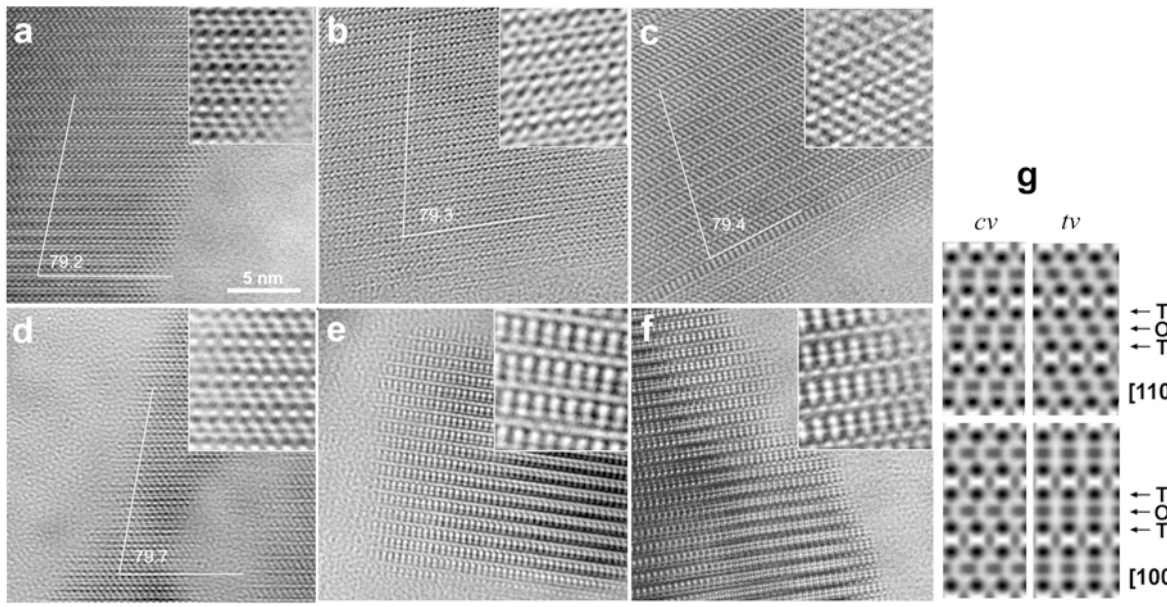


Figure 6. (a–f) Several HRTEM images from Canada illite recorded along the (a–d) [110] and (e, f) [100] directions. In (a–d), the measured angle between the (001) and (1$\bar{1}$0) planes is shown. The inset at the top-right in each figure is a magnified portion of the figure to show the detailed contrast of the image. (g) Simulated HRTEM contrast of *cv* and *tv*-1*M* illite along the [110] and [100] directions. The thickness and defocus values for the simulation are 2.5 nm and −42 nm, respectively.

setting the crystal orientation. In the present samples, the sizes of the celadonite and illite crystals were so small that the electrons were considerably radiated over the entire crystal during orientation setting before recording the SAED patterns. Another possible solution is to reduce the rate of dehydroxylation. For instance, an environmental cell in TEM to keep H_2O fugacity to a certain level may prevent or delay the dehydroxylation (Kohyama *et al.*, 1978). However, such an instrument degrades the resolution of imaging or inhibits the two-axis tilting of specimens.

Conversely, the present results are valuable as direct evidence for the cation migration in the 2:1 layer by its dehydroxylation. This idea was presented previously (*e.g.* Drits *et al.*, 1995) but was derived only from the change of cell parameters and intensity profiles in powder XRD patterns. The observed cation migration in TEM confirms the theoretical consideration for the origin of cation migration accompanying dehydroxylation. However, as described above, careful analyses of the HRTEM contrasts revealed structural features that are not explained by the results of the heating experiments. Figures 2–4 suggest that the new cation arrangement in celadonite from the [100] imaging is the fully occupied M1 site and the half-occupied M2 and M3 sites, consistent with the distribution of octahedral cations in the averaged *cv* unit cell of the dehydroxylated celadonite determined by Muller *et al*. (2000a). Those authors assumed, however, that the actual *cv*-like layer is not centro-symmetric, that "left-handed" and "right-handed" fragments can form, and that either the M2 or M3 site is always vacant in each fragment. If the size of the fragments is small, the two fragments may be averaged in a wider range, which results in the half occupancy for M2 and M3 sites. On the contrary, if this structure model is realized, the HRTEM contrast at a very thin region of the specimen may show the contrast without the mirror plane normal to the *b* axis, as shown in Figure 3b. However, such contrast is not observed in the thin regions in Figure 2. This result may indicate that the size of the fragments is very small, probably on the order of a few unit cells, or such fragments actually may not exist in the present specimen.

On the other hand, the HRTEM contrast along the [1$\bar{1}$0] direction cannot be explained by the cation distribution with the M1 site fully occupied. One may try to find a more complex cation distribution to explain this disagreement, but the HRTEM images also indicate that the configuration of the two T sheets in the 2:1 layer is preserved as in the natural state. Hence, the assumption that the arrangement of the cation sites between the two T sheets is close to that in the natural state, where the sites are hexagonally arranged, seems reasonable. With this assumption, no cation distribution can be found which reproduces the two HRTEM contrasts simultaneously. An explanation for the disagreement is that cation distribution is actually different depending on whether the crystals are tilted with either the [100] or the [1$\bar{1}$0] direction parallel to the electron beam. One should keep in mind that the crystal observed by TEM is not representative of the bulk but rather of a sample processed to a thin foil; dehydroxylation and

https://doi.org/10.1346/CCMN.2010.0580407 Published online by Cambridge University Press

subsequent cation migration do occur in such a processed specimen. Crystals observable along the [100] direction are thin along [100] whereas those observable along the [1$\bar{1}$0] are thin along [1$\bar{1}$0], with a thickness of <10 nm which is almost the limit to obtain such HRTEM images with no contrast reversal, as shown here. In other words, the two crystals have different morphologies and suspecting that the way of cation migration by dehydroxylation is different depending on such morphologies may not be unreasonable.

CONCLUSIONS

Unexpected contrasts at the octahedral sheet in the HRTEM images from celadonite and *cv*-illite are ascribed to cation migration after dehydroxylation which is induced by electron radiation in TEM. This phenomenon makes HRTEM recording of these minerals in the natural state extremely difficult. The investigation of phyllosilicates that contain *cv* 2:1 layers by HRTEM in particular will be difficult without some new technique for TEM. In contrast, the present results support the previous works which suggested the cation migration in dehydroxylated celadonite and *cv*-illite by heating.

ACKNOWLEDGMENTS

The authors are grateful to E. Okunishi from JEOL, Ltd., for supporting the Cs-corrected HAADF-STEM experiment. VAD thanks the Russian Foundation of Fundamental Research.

REFERENCES

Altaner, S.P. and Ylagan, R.F. (1997) Comparison of structural models of mixed-layer illite-smectite and reaction mechanisms of smectite illitization. *Clays and Clay Minerals*, **45**, 517–533.

Capitani, G.C., Oleynikov, P., Hovmoller, S., and Mellini, M. (2006) A practical method to detect and correct for lens distortion in the TEM. *Ultramicroscopy*, **106**, 66–74.

Comodi, P. and Zanazzi, P.F. (2000) Structural thermal behaviour of paragonite and its dehydroxylate: a high-temperature single-crystal study. *Physics and Chemistry of Minerals*, **27**, 377–385.

Cuadros, J. and Altaner, S.P. (1998a) Characterization of mixed-layer illite-smectite from bentonites using microscopic, chemical and X-ray methods: constraints on the smectite-to-illite transformation mechanism. *American Mineralogist*, **83**, 762–774.

Cuadros, J. and Altaner, S.P. (1998b) Compositional and structural features of the octahedral sheet in mixed-layer illite-smectite from bentonites. *European Journal of Mineralogy*, **10**, 111–124.

Drits, V.A. (2003) Structural and chemical heterogeneity of layer silicates and clay minerals. *Clay Minerals*, **38**, 403–432.

Drits, V.A., Plançon, A., Sakharov, B.A., Besson, G., Tsipursky, S.I., and Tchoubar, C. (1984) Diffraction effects calculated for structural models of K-saturated montmorillonite containing different types of defects. *Clay Minerals*, **19**, 541–562.

Drits, V.A., Weber, F., Salyn, A., and Tsipursky, S. (1993) X-ray identification of 1*M* illite varieties: Application to the study of illites around uranium deposits of Canada. *Clays and Clay Minerals*, **41**, 389–398.

Drits, V.A., Besson, G., and Muller, F. (1995) An improved model for structural transformations of heat-treated aluminous dioctahedral 2:1 layer silicates. *Clays and Clay Minerals*, **43**, 718–731.

Drits, V.A., Salyn, A.L., and Šucha, V. (1996) Structural transformations of interstratified illite-smectites from Dolna Ves hydrothermal deposits: dynamics and mechanisms. *Clays and Clay Minerals*, **44**, 181–190.

Drits, V.A., Sakharov, B.A., Dainyak, L.G., Salyn, A.L., and Lindgreen, H. (2002) Structural and chemical heterogeneity of illite-smectites from Upper Jurassic mudstones of East Greenland related to volcanic and weathered parent rocks. *American Mineralogist*, **87**, 1590–1607.

Drits, V.A., Lindgreen, H., Sakharov, B.A., Jakobsen, H.J., and Zviagina, B.B. (2004) The detailed structure and origin of clay minerals at the Cretaceous/Tertiary boundary, Stevns Klint (Denmark). *Clay Minerals*, **39**, 367–390.

Drits V.A., McCarty, D.K., and Zviagina, B.B. (2006) Crystal-chemical factors responsible for the distribution of octahedral cations over *trans*- and *cis*-sites in dioctahedral 2:1 layer silicates. *Clays and Clay Minerals*, **54**, 131–152.

Drits, V.A., Lindgreen, H., Sakharov, B.A., Jakobsen, H.J., Fallick, A.E., Salyn, A.L., Dainyak, L.G., Zviagina, B.B., and Barfod, D.N. (2007) Formation and transformation of mixed-layer minerals by Tertiary intrusives in Cretaceous mudstones, West Greenland. *Clays and Clay Minerals*, **55**, 261–284.

Emmerich, K., Wolters, F., Kahr, G., and Lagaly G. (2009) Clay profiling: The classification of montmorillonites. *Clays and Clay Minerals*, **57**, 104–114.

Ferraris, G. and Ivaldi, G. (2002) Structural features of micas. Pp. 117–148 in: *Micas: Crystal Chemistry and Metamorphic Petrology* (A. Mottana, F.P. Sassi, J.B. Thompson Jr. and S. Guggenheim, editors). Reviews in Mineralogy and Geochemistry Vol. **46**, Mineralogical Society of America, Washington, D.C.

Kilaas, R. (1998) Optimal and near-optimal filters in high-resolution electron microscopy. *Journal of Microscopy*, **190**, 45–51.

Kimbara, K. and Shimoda, S. (1973) A ferric celadonite in amygdales of dolerite at Taiheizan, Akita prefecture, Japan. *Clay Science*, **4**, 143–150.

Kogure, T. (2002) Investigation of micas using advanced TEM. Pp. 281–310 in: *Micas: Crystal Chemistry & Metamorphic Petrology* (A. Mottana, F.P. Sassi, J.B. Thompson, Jr. and S. Guggenheim, editors). Reviews in Mineralogy and Geochemistry, Vol. **46**, Mineralogical Society of America, Washington, D.C.

Kogure, T. (2007) Imaging of dioctahedral 2:1 layers by high-resolution transmission electron microscopy (HRTEM): Possibility of recording the dehydroxylate. *American Mineralogist*, **92**, 1368–1373.

Kogure, T., Eilers, P.H.C., and Ishizuka, K. (2008a) Application of optimum HRTEM noise filters in mineralogy and related sciences. *Microscopy and Analysis*, **22**, S11–S14.

Kogure, T., Kameda, J., and Drits, V.A. (2008b) Stacking faults with 180º layer rotation in celadonite, an Fe- and Mg-rich dioctahedral mica. *Clays and Clay Minerals*, **56**, 612–621.

Kohyama, N., Fukushima, K., and Fukami, A. (1978) Observation of hydrated form of tubular halloysite by an electron microscope equipped with an environmental cell. *Clays and Clay Minerals*, **26**, 25–40.

Krivanek, O.L., Dellby, N., and Lupini, A.R. (1999) Towards sub-angstrom electron beams. *Ultramicroscopy*, **78**, 1–11.

Lanson, B., Beaufort, D., Berger, G., Baradat, J., and

https://doi.org/10.1346/CCMN.2010.0580407 Published online by Cambridge University Press

Lacharpagne, J.C. (1996) Illitization of diagenetic kaolinite-to-dickite conversion series: Late-stage diagenesis of the Lower Permian Rotliegend sandstone reservoir, offshore of the Netherlands. *Journal of Sedimentary Research*, **66**, 501–518.

Lee, M. (1996) 1*M* (cis) illite as an indicator of hydrothermal activities and its geological implication. 33rd Annual meeting of the Clay Minerals Society, program and abstracts, June 15–20, 1996, Gatlinburg, Tennessee, USA, p. 106.

Lindgreen, H., Drits, V.A., Sakharov, B.A., Salyn, A.L., Wrang, P., and Dainyak, L.G. (2000) Illite-smectite structural changes during metamorphism in black Cambrian Alum shales from the Baltic area. *American Mineralogist*, **85**, 1223–1238.

Lindgreen, H., Drits, V.A., Sakharov, B.A., Jakobsen, H., Salyn, A.L., Dainyak, L.G., and Kroyer, H. (2002) The structure and diagenetic transformation of illite-smectite and chlorite-smectite from North Sea Cretaceous-Tertiary chalk. *American Mineralogist*, **87**, 429–450.

Marks, L.D. (1996) Wiener-filter enhancement of noisy HREM images. *Ultramicroscopy*, **62**, 43–52.

McCarty, D.K. and Reynolds R.C., Jr. (1995) Rotationally disordered illite-smectite in Paleozoic K-bentonites. *Clays and Clay Minerals*, **43**, 271–284.

McCarty, D.K. and Reynolds R.C., Jr. (2001) Three-dimensional crystal structures of illite-smectite minerals in Paleozoic K-bentonites from the Appalachian basin. *Clays and Clay Minerals*, **49**, 24–35.

McCarty, D.K., Sakharov, B.A. and Drits, V.A. (2008) Early clay diagenesis in Gulf Coast sediments: new insights from XRD profile modeling. *Clays and Clay Minerals*. **56**, 359–379.

Méring, J. and Oberlin, A. (1971) Smectites. Pp. 193–229 in: *The Electron-Optical Investigation of Clays* (J.A. Gard, editor). Mineralogical Society, London.

Muller, F., Drits, V.A., Plançon, A., and Besson, G. (2000a) Dehydroxylation of Fe^{3+}, Mg-rich dioctahedral micas: (I) structural transformation. *Clay Minerals*, **35**, 491–504.

Muller, F., Drits, V.A., Plançon, A., and Robert, J.-L. (2000b) Structural transformation of 2:1 dioctahedral layer silicates during dehydroxylation-rehydroxylation reactions. *Clays and Clay Minerals*, **48**, 572–585.

Pennycook, S.J. and Jesson, D.E. (1990) High-resolution incoherent imaging of crystals. *Physical Review Letters*, **64**, 938–941.

Reynolds, R.C., Jr. (1993) Three-dimensional X-ray diffraction from disordered illite: simulation and interpretation of the diffraction patterns. Pp. 44–78 in: *Computer Applications to X-ray Diffraction Methods* (R.C. Reynolds and J. Walker, editors). Workshop Lectures Series, **5**, The Clay Minerals Society, Bloomington, Indiana, USA.

Reynolds, R.C., Jr. and Thomson, C.H. (1993) Illites from the Potsdam sandstone of New York, a probable noncentrosymmetric mica structure. *Clays and Clay Minerals*, **41**, 66–72.

Rieder, M., Cavazzini, G., D'yakonov, Yu.S., Frank-Kamenetskii, V.A., Gottardi, G., Guggenheim, S., Koval', P.V., Müller, G., Neiva, A.M.R., Radoslovich, E.W., Robert, J.L., Sassi, F.P., Takeda, H., Weiss, Z., and Wones, D.R. (1999) Nomenclature of the micas. *Mineralogical Magazine*, **63**, 267–279.

Sainz-Diaz, C.I., Hernandez-Laguna, A., and Dove, M.T. (2001) Theoretical modeling of cis-vacant and trans-vacant configurations in the octahedral sheet of illites and smectites. *Physics and Chemistry of Minerals*, **28**, 322–331.

Tsipursky, S.I., and Drits, V.A. (1984) The distribution of octahedral cations in the 2:1 layers of dioctahedral smectites studied by oblique-texture electron diffraction. *Clay Minerals*, **19**, 177–193.

Tsipursky, S.I. and Drits, V.A. (1986) Refinement of the crystal structure of celadonite. *Mineralogichesky Jurnal*, **8**, 32–40 (in Russian).

Udagawa, S., Urabe, K., and Hasu, H. (1974) The crystal structure of muscovite dehydroxylate. *Japanese Association of Mineralogy, Petrology and Economic Geology*, **69**, 381–389.

Wardle, R. and Brindley, G.W. (1972) The crystal structures of pyrophyllite, 1Tc and of its dehydroxylate. *American Mineralogist*, **57**, 732–750.

Wolters, F., Lagaly, G., Kahr, G., Nueesch, R., and Emmerich, K. (2009) A comprehensive characterization of dioctahedral smectites. *Clays and Clay Minerals*, **57**, 115–133.

Ylagan, R.F., Altaner, S.P., and Pozzuoli, A. (2000) Reaction mechanisms of smectite illitization associated with hydrothermal alteration from Ponza Island, Italy. *Clays and Clay Minerals*, **48**, 610–631.

Zhukhlistov, A.P. (2005) Crystal structure of celadonite from the electron diffraction data. *Crystallography Reports*, **50**, 902–906.

Zhukhlistov, A.P., Zvyagin, B.B., Lazarenko, E.K., and Pavlishin, V.I. (1977) Refinement of an iron celadonite structure. *Kristallographya*, **22**, 498–505 (in Russiam) [*Soviet Physics and Crystallography*, **22**, 284–290].

Zhukhlistov, A.P., Dragulesku, E.M., Rusinov, V.L., Kovalenker, V.A., Zvyagin, B.B., and Kuz'mina, O.V. (1996) Sericite with non centrosymmetric structure from gold-silver-polymetallic ores of Banska Stiavnica deposit (Slovakia). *Zapiski Vserossiyskogo Mineralogicheskogo Obshchestva*, **125**, 47–54 (in Russian).

Zvyagin, B.B., Rabotnov, V.T., Sidorenko, O.V., and Kotelnikov, D.D. (1985) Unique mica consisting of non-centrosymmetric layers. *Izvestiya Akademii Nauk S.S.S.R, Seriya Geologicheskaya*, **35**, 121–124 (in Russian).

(*Received 18 January 2010; revised 2 June 2010; Ms. 401; A.E. M.A. Velbel*)

https://doi.org/10.1346/CCMN.2010.0580407 Published online by Cambridge University Press